Langmuir

Article

pubs.acs.org/Langmuir

Facile Synthesis of $ZnFe_2O_4$ Nanoparticles with Tunable Magnetic and Sensing Properties

Peizhi Guo,*[,†,‡] Lijun Cui,[†,‡] Yiqian Wang,*[,†] Meng Lv,[†,‡] Baoyan Wang,[†,‡] and X. S. Zhao[†,‡,§]

[†]Laboratory of New Fiber Materials and Modern Textile, the Growing Base for State Key Laboratory, Qingdao University, Qingdao 266071, P. R. China

[‡]School of Chemistry, Chemical Engineering and Environment, Qingdao University, Qingdao 266071, P. R. China

[§]School of Chemical Engineering, The University of Queensland, St. Lucia, QLD 4072, Australia

Supporting Information

ABSTRACT: Nanoparticles (NPs) and colloidal nanocrystal clusters (CNCs) of $ZnFe_2O_4$ were synthesized by using a solvothermal method in a controlled manner through simply adjusting the solvents. When a glycerol/water mixture was used as the solvent, $ZnFe_2O_4$ NPs were obtained. However, using ethylene glycol solvent yielded well-dispersed $ZnFe_2O_4$ CNCs. X-ray diffraction (XRD) and transmission electron microscopy (TEM) data confirmed that the $ZnFe_2O_4$ NPs were a single crystalline phase with tunable sizes ranging from 12 to 20 nm, while the $ZnFe_2O_4$ CNCs of submicrometer size consisted of single-crystalline nanosheets. Magnetic measurement results showed that the $ZnFe_2O_4$ NPs were ferromagnetic with a very small hysteresis loop at room temperature. However, CNCs displayed a superparamagnetic behavior due to preferred orientations of the nanosheets. Electrochemical sensing properties showed that both the size of the NPs and the structure of the CNCs had a great influence on their electrochemical properties in the reduction of H_2O_2. Based on the experimental results, the formation mechanisms of both the $ZnFe_2O_4$ CNCs and NPs as well as their structure−property relationship were discussed.

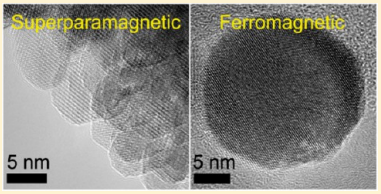

1. INTRODUCTION

Spinel ferrites have attracted great attention because of their broad applications in many fields, such as magnetic materials, energy, biomedicine, and diverse catalytic processes.[1−3] As the shape, size, and structure of the materials have great influences on their chemical and physical properties when the dimension is reduced to the nanometer scale, nanostructured materials can show unique optical, electrical, magnetic, and catalytic properties, which are quite different from that of the bulk counterpart.[4] Therefore, controlled synthesis of nanometer-sized materials is of great importance for investigating the structure−property relationship of the nanomaterials.[5−8] So far, ferrite nanomaterials with various structures have been prepared through different synthetic methods, such as the hydrothermal/solvothermal methods, sol−gel method, and template method.[5−20] For instance, homogeneous hollow core−shell microspheres of spinel ferrites (MFe_2O_4, M = Zn, Co, Ni, Cd) have been obtained by using carbonaceous saccharide microspheres as template.[16] Submicrometer ferromagnetic ferrite spheres with single crystalline structures were synthesized by a solvothermal method and displayed excellent colloidal stability in aqueous solutions.[19] Porous "timber-like" $ZnFe_2O_4$ superstructures have been prepared by calcining the zinc ferrioxalate precursor.[20] Recently, $ZnFe_2O_4$ has also received great interest due to the wide applications in magnetic material, adsorption, photocatalysis, and solar cells.[13,19−23] For example, magnetic $ZnFe_2O_4$ nanoparticles can be used as colorimetric biosensors for the detection of urine glucose due to its intrinsic peroxidase-like activity of the nanoparticles.[21] $ZnFe_2O_4$ nanorods exhibited a good photocatalytic activity toward the decomposition of methylene blue.[13] However, controlled synthesis of ferrite nanomaterials with tunable morphologies, structures, and properties is still challenging.

Magnetic nanomaterials, especially superparamagnetic iron series materials, have great potentials in magnetic resonance imaging (MRI), separation and purification, drug delivery, and magnetically induced hyperthermia.[1,24−26] However, superparamagnetic materials usually show a low magnetization value, which limits their practical applications. Increasing nanocrystal size is one way to increase the saturation magnetization (M_s).[3] However, a superparamagnetic−ferromagnetic transition occurs at a critical size.[8] So magnetic nanocrystals that show superparamagnetic behavior with crystal size larger than the critical size at which the transition occurs are desired.[3] Forming colloidal nanocrystal clusters (CNCs) has proved to be an effective way to retain superparamagnetic behavior with high magnetization.[27] The formulation of the synthesis protocol is a key to the preparation of targeted magnetic materials.[9−20] Among the synthetic methods reported, the solvothermal method has proved feasible to synthesize nanomaterials with controllable morphology and microstructure.[7−9,28,29] For solvothermal synthesis, the factors including the solvents, reactants, and synthesis procedure can be regulated easily to prepare a desired nanostructure. For

Received: April 29, 2013
Revised: June 20, 2013
Published: June 20, 2013

   dx.doi.org/10.1021/la401627x | Langmuir 2013, 29, 8997−9003

example, magnetite CNCs can show superparamagnetic behavior with large M_s values, in which the size of CNCs can be adjusted in the range of 30−180 nm by controlling the concentration of sodium hydroxide in the starting systems.[8] Recently, we used the solvothermal method to prepare submicrometer superparamagnetic $MnFe_2O_4$ CNCs with the M_s value larger than that of $MnFe_2O_4$ nanocrystals.[7] Despite the recent research progress, the structural nature of nanosized magnetic materials deserves further elucidations.

In this paper, submicrometer superparamagnetic $ZnFe_2O_4$ CNCs and size-tunable ferromagnetic $ZnFe_2O_4$ nanoparticles (NPs) were synthesized by using a one-step solvothermal method through rational design. It was found that CNCs were composed of single-crystalline nanosheets with highly preferred orientations, showing a magnetization saturation value as high as 25.4 emu/g. The magnetic properties including magnetization saturation, remnant magnetization, and coercivity of the $ZnFe_2O_4$ NPs were found to be dependent upon the size of the NPs. Electrochemical sensing properties of the $ZnFe_2O_4$ CNCs and NPs were also studied using the reaction of electrochemical reduction of hydrogen peroxide.

2. EXPERIMENT

2.1. Materials. All chemicals, including $FeCl_3·6H_2O$, $ZnCl_2$, CH_3COONa, ethylene glycol, glycerol, hydrogen peroxide, and ethanol, were of analytical grade (Sinopharm Chemical Reagent Co.) and used as received. Double distilled water was used in the experiments.

2.2. Synthesis of $ZnFe_2O_4$ Nanoparticles. In a typical synthesis, 15 mL of ethylene glycol (EG) solution of $FeCl_3·6H_2O$ (0.54 g) and 15 mL of EG solution of $ZnCl_2$ (0.14 g) were mixed, and then CH_3COONa (0.8 g) was added into the mixture under vigorous stirring. The homogeneous mixture was transferred into a 40 mL Teflon-lined autoclave, which was then tightly sealed and heated at 200 °C for 12 h in an oven. Subsequently, the autoclave was allowed to cool down to room temperature. The solid products were collected by centrifugation, washed separately with distilled water and ethanol for several times, and then dried in an oven at 60 °C for 6 h. The final solid product is named CNCs. The procedure for the preparation of $ZnFe_2O_4$ NPs was the same as that of CNCs, except for the use of the mixed solvent composed of glycerol and deionization water with volume ratio of 1:1.

2.3. Characterization. Powder X-ray diffraction (XRD) patterns were recorded on a Bruker D8 Advance X-ray diffractometer equipped with graphite monochromatized Cu Kα radiation (λ = 0.154 18 nm) from 10° to 80° (2θ). Transmission electron microscopy (TEM) and high-resolution TEM (HRTEM) images were collected on a JEOL JEM2010 TEM operated at 200 kV. Energy dispersive X-ray spectroscopy (EDS) was performed on a JEOL JEM2010 TEM, and electron energy-loss spectroscopy (EELS) was carried out on a FEI Tecnai F20 TEM. Magnetic properties were measured using a LDJ9500 vibrating sample magnetometer (VSM) at room temperature.

2.4. Electrochemical Sensing Measurement. Electrochemical sensing measurements were performed on a CHI760C electrochemical workstation using a three-electrode cell. Platinum wire and saturated calomel electrode were used respectively as counter electrode and reference electrode in aqueous phosphate buffer solutions (PBS, 0.1 M, pH 7.4). $ZnFe_2O_4$-modified gold disk electrodes (3 mm in diameter) were used as the working electrode. A 10 μL aliquot of $ZnFe_2O_4$ suspension (1 mg mL^{-1}) ultrasonicated for 30 min was uniformly cast onto the surface of the gold electrode. The modified electrode was dried under ambient conditions before being used. Different amounts of H_2O_2 were injected into the phosphate buffer solution, and the experiments were conducted in a thoroughly anaerobic condition by bubbling with high-purity N_2 for 15 min.

3. RESULTS AND DISCUSSION

3.1. Crystal Structure. Figure 1 shows the XRD patterns of the samples obtained with the synthesis time of 12 h. It can be found that the diffraction peaks match well with the standard pattern of cubic $ZnFe_2O_4$ with a spinel structure (JCPDS No. 77-0011). The peaks at 30.2°, 35.5°, 42.9°, 53.3°, 56.8°, and 62.3° 2θ can be indexed to (220), (311), (400), (422), (511), and (440) planes of spinel $ZnFe_2O_4$, respectively. The average crystal sizes of the $ZnFe_2O_4$ CNCs and NPs calculated from the Scherrer equation were about 10.4 and 19.7 nm, respectively, based on the measurements of the full width at half-maximum (fwhm) of the (311) peaks.

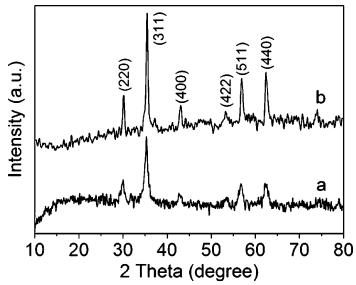

Figure 1. XRD patterns of $ZnFe_2O_4$ CNCs (a) and NPs (b).

3.2. Morphology and Microstructure. The morphology and microstructure of the $ZnFe_2O_4$ samples were investigated by TEM and HRTEM (Figures 2 and 3). As depicted in Figure 2A, the appearance of individual spheres as well as the dark areas among the overlapping samples confirmed the well-separated submicrometer spherical structures of $ZnFe_2O_4$ CNCs. The size of the $ZnFe_2O_4$ CNCs was about 450 nm, as shown in the inset in Figure 2A, by counting more than 300 individual particles. The crystalline nature of the sample can be derived from the selected area electron diffraction (SAED) pattern of a single particle (Figure 2B). The appearance of the bright arc in the diffraction circle in the SAED pattern of a single CNC indicated that the spherical structures were formed by $ZnFe_2O_4$ nanocrystals in highly preferred orientations, and slight misalignments existed among the primary nanocrystals.[7,8] According to the bright-field TEM image of a single cluster (Figure 2C), obviously rough surface should express the unique structure for the separated CNCs. As shown in Figure 2D, the HRTEM image of an edge of an individual particle boxed in Figure 2C showed that CNCs formed by the assembly of $ZnFe_2O_4$ nanosheets with dimensions of about 10 nm (Figure S1). This value was in good agreement with the XRD results (Figure 1a). Moreover, the parallel lattice fringes observed in the nanosheets in Figure 2D further proved that they adopted perfectly orientated attachment.[30] HRTEM images shown in Figure 2D,E and Figure S1 also confirmed the single-crystalline nature of the primary nanosheets. As depicted in Figure 2E, the atomic lattice fringes can be clearly observed, and the interplanar spacings were measured to be 2.68 and 2.99 Å, which were close to the {311} and {022} lattice planes of cubic $ZnFe_2O_4$, respectively. The angle between the crystalline planes observed in Figure 2E was 64.7°, in good agreement with the theoretical value.

Figure 2F shows the electron energy-loss spectroscopy (EELS) results. The thickness of the nanosheets was about 5.2 nm calculated from the formula $t = \lambda \ln(I_0/I_t)$,[31] where t = thickness of the nanosheets, λ= inelastic mean free path, I_0 =

dx.doi.org/10.1021/la401627x | Langmuir 2013, 29, 8997−9003

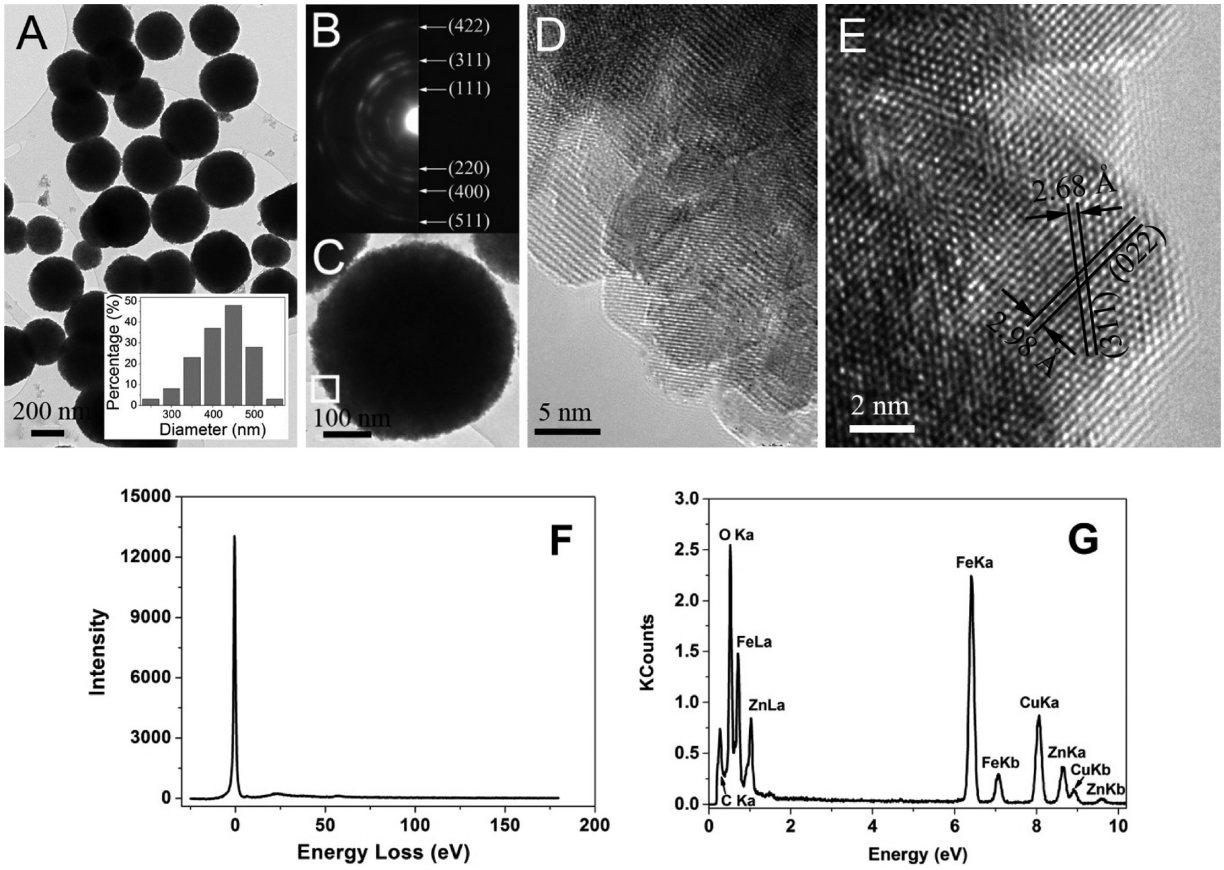

Figure 2. TEM images (A, C), SAED pattern (B), and HRTEM images (D, E) of $ZnFe_2O_4$ CNCs. The inset in (A) is the size distribution of CNCs. (F) EELS spectrum of the nanosheets. (G) EDS spectrum acquired from a single CNC in (A).

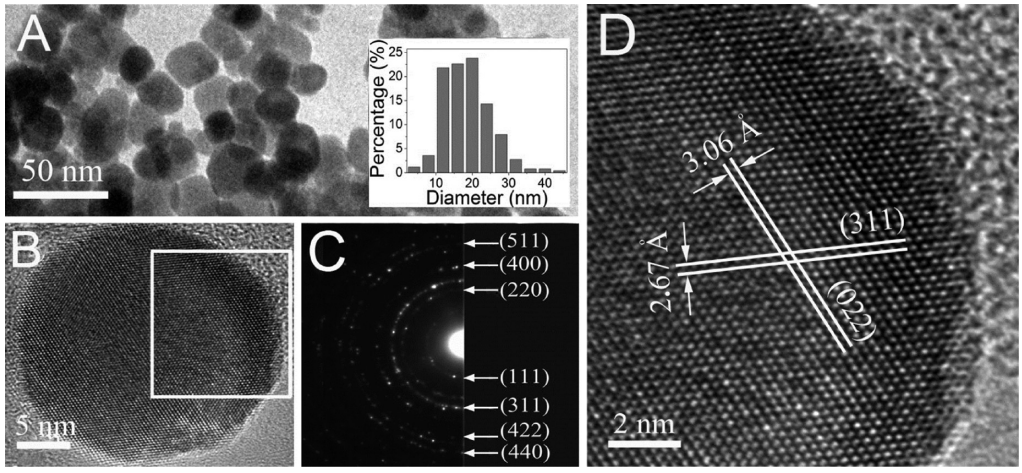

Figure 3. TEM image (A), SAED pattern (C), and HRTEM images (B, D) of $ZnFe_2O_4$ NPs. The inset in (A) is the size distribution of NPs.

zero-loss peak, and I_t = total specturm. Energy dispersive X-ray spectroscopy (EDS) results from a single CNC showed that it was mainly composed of Zn, Fe, and O (Figure 1G). Quantification of the EDS spectrum showed that the ratio of Zn, Fe, and O was about 1:2:4, suggesting that the CNCs had a chemical formula of $ZnFe_2O_4$.

When the solvent of the synthesis system was replaced by a mixture of glycerol and water, $ZnFe_2O_4$ NPs were obtained (Figure 3A). The average size of these NPs was about 20 nm as illustrated in the inset of Figure 3A, which was also consistent with the XRD results (Figure 1b). Some agglomerated NPs formed probably because of magnetic dipole interactions between NPs[32] and/or high surface energy of NPs. The SAED pattern showed some circle rings (Figure 3C), which can be well indexed to a cubic $ZnFe_2O_4$ phase. However, the SAED pattern was mainly composed of bright diffraction spots because it was obtained from many particles, indicating the well-crystalline nature of $ZnFe_2O_4$ NPs. This can be confirmed by the HRTEM characterization of a single NP (Figure 3B), in which single-crystalline nature of the $ZnFe_2O_4$ NPs was clearly observed. Figure 3D shows a magnified HRTEM image of the boxed region in Figure 3C. The spacings between the lattice

dx.doi.org/10.1021/la401627x | Langmuir 2013, 29, 8997−9003

fringes shown in Figure 3D are 2.67 and 3.16 Å, which agree well with {311} and {022} planar spacings of cubic $ZnFe_2O_4$, respectively. Furthermore, the measured angle between these two planes is 64.1°, verifying the formation of cubic $ZnFe_2O_4$ phase. Furthermore, the EDS data of a single NP (Figure S2) also confirmed the chemical formula of $ZnFe_2O_4$ for NPs.

3.3. Evolution of the Intermediates. The intermediate products of these two different synthesis systems were collected and characterized by TEM (Figure 4) and XRD (Figure S3).

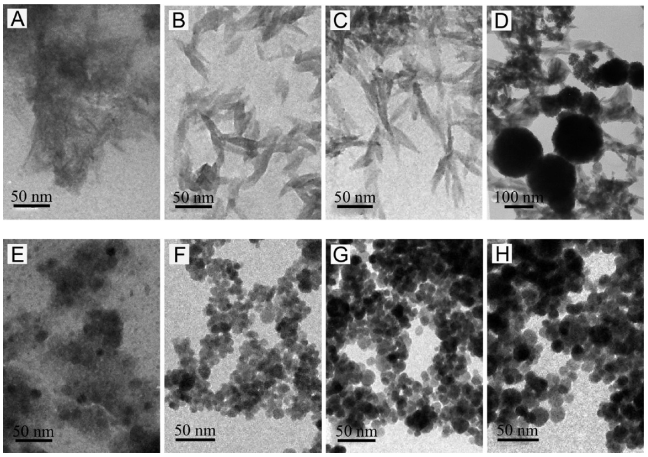

Figure 4. TEM images of the intermediates prepared from the EG (A–D) and mixed solvent (E–H) systems at 1 h (A, E), 2 h (B, F), 4 h (C, G), and 6 h (D, H).

The color change of these intermediate products can be clearly observed. For the EG system aimed to synthesize $ZnFe_2O_4$ CNCs, the intermediates were tan with the synthesis time no more than 4 h and then turned to dark brown with increasing the reaction time. However, the products turned black after solvothermal treatment for more than 2 h for the mixed solvent system. For the EG system, the sample obtained after 1 h of reaction was amorphous with irregular shapes as can be seen from Figure S3Aa and Figure 4A. After being heated for 2 h, amorphous spindle structures were obtained, as shown in Figure 4B and Figure S3Ab. The sample maintained a spindle shape after 4 h of reaction (Figure 4C). Particle aggregation is obvious. The XRD pattern of the sample obtained after 4 h of reaction (Figure S3Ac) can be indexed to a tetragonal akaganeite phase (β-FeOOH, JCPDS No. 75-1594), which is in accordance with the color of the product. Spherical $ZnFe_2O_4$ aggregates with a large size distribution formed with the synthesis time up to 6 h (Figure 4D). This can be verified by the XRD pattern (Figure S3Ad) in which a sharp peak at 35.5°, ascribed to the (311) plane of cubic $ZnFe_2O_4$ phase (JCPDS No. 77-0011), was observed. In the meantime, spindle structures almost disappeared. Small NPs were also observed and some gradually assembled to spherical-like aggregates. The main driving force for the aggregation of NPs can be generally attributed to van der Waals force and electrostatic interactions as well as the tendency for reducing the high surface energy through both the attachments among the primary NPs and the rotation of these primary NPs to give coherent lattice structure at grain boundaries.[33−37] The formation of these spheres could be ascribed to the expense of small particles on the basis of Ostwald ripening.[38] Finally, nearly monodispersed $ZnFe_2O_4$ CNCs were obtained after 12 h reaction (Figure 2A).

For the mixed solvent system, mainly small particles were observed for the sample collected after 1 h (Figure 4F). The XRD result (Figure S3Ba) revealed this sample was poorly crystalline. After being heated for 2 h, nearly monodispersed NPs were observed, and all the peaks of the XRD patterns (Figure S3B) can be assigned to the standard pattern of cubic $ZnFe_2O_4$ phase (JCPDS No. 77-0011). The morphology of the sample changed slightly within 2−6 h (Figure 4F−H). But the particle size increased with the augment of reaction time, and the average particle sizes were 11.6, 16.2, and 20.5 nm for the samples collected at the reaction time of 2, 6, and 12 h, respectively. Namely, the size of $ZnFe_2O_4$ NPs can be easily regulated by simply adjusting the reaction time. The formation of $ZnFe_2O_4$ NPs could be explained as quick nucleation occurred, and the growth process reached a balance before small particles could assemble into spherical aggregates.[39] The existence of water in the solvent should improve the hydrolysis of metal ions at a relative high hydrothermal temperature,[3] and addition of glycerol may inhibit the aggregation of nanoparticles. With the synthesis time elongated to 4 h or more, the nanocrystal growth was dominated by the Ostwald ripening process in which the formation of larger nanocrystals was ascribed to the dissolution of smaller nanocrystals with high surface energy.[40] Thus, the sample prepared in mixed solvents only consisted of NPs.

On the basis of the experimental results, it can be concluded that the formation mechanisms of $ZnFe_2O_4$ CNCs and nanoparticles are different (Scheme 1). The solvents can

Scheme 1. Schematic Illustration for the Formation of $ZnFe_2O_4$ CNCs and NPs

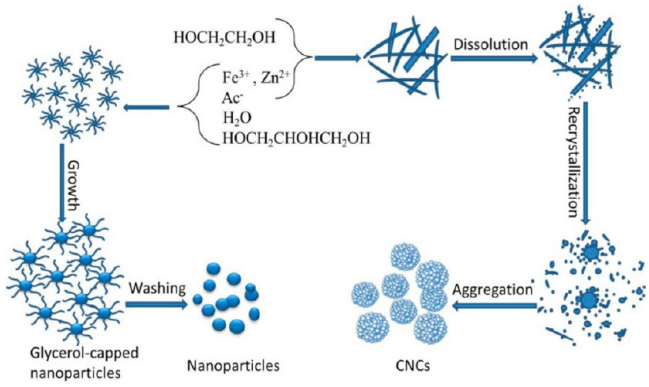

influence the hydrolysis of the reagents and crystal growth of the targeted nanomaterials because of their molecular structures, different solubility, viscosity, density, diffusivity, and other heat and mass transport-related properties.[41] The Ostwald ripening process also plays an important role in the formation of nanocrystals for both systems. For the synthesis of CNCs, it is suggested that the existence of sodium acetate in EG systems should favor the hydrolysis of ferric ions due to the existence of crystalline water in the started iron source, which can be deduced from the XRD patterns and color variations of the intermediates. Furthermore, EG might form chelates with metal ions, which led to the decrease of the hydrolysis reaction rate. A slow hydrolysis reaction rate should compensate for the formation of spindle structures.[13] The decomposition of the chelates might produce water into the system. Both the solubility of the precursors and hydrolysis of metal ions were increased with the appearance of water. The primary crystals

dx.doi.org/10.1021/la401627x | Langmuir 2013, 29, 8997−9003

were formed through dehydration under high temperature. Large particles were gradually formed with the elongation of synthesis time due to the Ostwald ripening. Furthermore, the particles with similar sizes repelled one from another,[8,41] which led to the formation of separated CNCs, as shown in Scheme 1. For the synthesis of $ZnFe_2O_4$ NPs, glycerol served as the solvent and stabilization agent (Scheme 1). The presence of water induced the quick hydrolysis process of both metal ions at elevated temperature, which contributed to the quick nucleation, and the glycerol molecules capping on the surface of particles inhibited the growth process and aggregation among NPs. Therefore, separated particles with controllable sizes can be obtained without aggregation via control over the synthesis time. The formations of $ZnFe_2O_4$ NPs and CNCs were similar to those of magnetite and ferrite structures.[27]

3.4. Magnetic Characterization. Magnetic properties of $ZnFe_2O_4$ samples were measured at room temperature at a magnetic field of $H = 1.4 \times 10^4$ Oe. Figure 5 shows

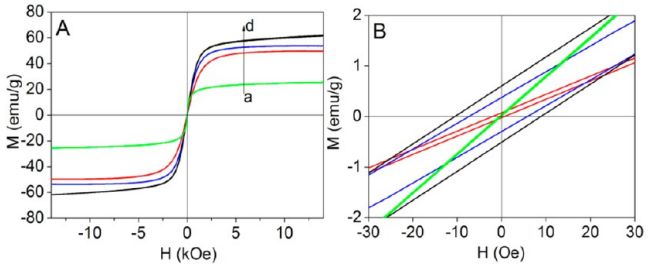

Figure 5. Magnetization hysteresis of $ZnFe_2O_4$ samples (A): CNCs (a) and NPs with the sizes of 11.6 nm (b), 16.2 nm (c), and 20.5 nm (d), and the magnified graph of A (B).

magnetization curves of $ZnFe_2O_4$ CNCs as well as three types of NPs with different sizes of 11.6, 16.2, and 20.5 nm at the full scale. As depicted in Figure 5B, all the $ZnFe_2O_4$ NPs presented very small hysteresis loops in the enlarged manner, indicating the ferromagnetic behavior for these samples. The values of saturation magnetization (M_s) were measured to be 49.3, 53.8, and 61.3 emu/g for $ZnFe_2O_4$ NPs with the sizes of 11.6, 16.2, and 20.5 nm, respectively. Namely, the M_s value increased with the nanoparticle size similar to those results reported in the literature.[3,6,40] NPs with the size of 11.6 nm showed the lowest remnant and coercivity among all the NP samples. These could be ascribed to the size effect of NPs.[6,8,42] Furthermore, the single crystalline nature of $ZnFe_2O_4$ NPs should contribute to the variation of magnetic properties with the size of the NPs.[3] It can also be expected the existence of the superparamagnetic−ferromagnetic transition with continuous decrease of particle size. However, submicrometer CNCs composed of small nanosheets were superparamagnetic with zero remnant and zero coercivity.[8,27] Generally, single-crystalline magnetic particles with the same size as those in CNCs exhibited ferromagnetic behavior. The superparamagnetic nature of $ZnFe_2O_4$ CNCs could be attributed to both the small size of primary crystalline nanosheets and their oriented attachment structure.[30,34] Furthermore, the magnetic interactions among crystallites were perturbed sufficiently.[23] The M_s value of CNCs was 25.4 emu/g higher than the reported values for $ZnFe_2O_4$ NPs at room temperature.[43,44] This should be ascribed to the unique structure of CNCs including the size, well-crystalline nature, and arrangement of the clusters. Namely, the assembly of $ZnFe_2O_4$ nanosheets endowed nanocrystal clusters with distinctive properties similar to those assemblies of CdTe NPs and Au nanocrystals.[45−47] However, the M_s value of CNCs was lower than that of NPs with the size of 11.6 nm probably because of the thin nature of primary nanosheets of $ZnFe_2O_4$.

3.5. Electrochemical Sensing Performance. $ZnFe_2O_4$ CNCs and NPs were explored to prepare biosensors toward the electrochemical reduction of H_2O_2.[48] Figure 6 shows the cyclic

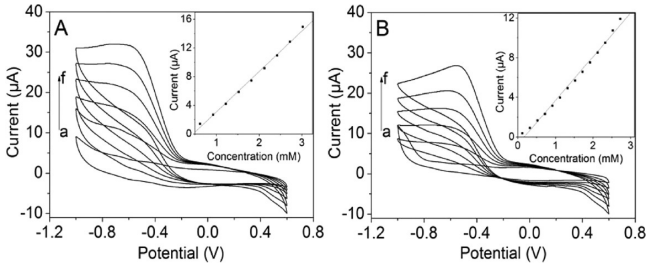

Figure 6. Cyclic voltammograms of $ZnFe_2O_4$-modified electrodes for CNCs (A) and NPs (B) at different H_2O_2 concentrations from (a) to (f): 0, 0.62, 1.22, 1.82, 2.42, and 3.02 mM.

voltammograms of the $ZnFe_2O_4$-modified gold electrodes in phosphate buffer solutions (PBS, pH 7.4) with the H_2O_2 concentrations of 0, 0.62, 1.22, 1.82, 2.44, and 3.02 mM. It can be seen that both samples show electrocatalytic activity toward the reduction of H_2O_2, and the peak currents increased gradually with the consecutive increase of H_2O_2 concentrations. For CNCs, the onset potentials for the reduction of H_2O_2 were −0.16 and −0.10 V for CNCs and NPs with the size of 11.6 nm, respectively, as shown in Figure 6A. It can also be derived that the maximum currents for CNCs and NPs were 14.9 and 16.9 μA at the potentials of −0.73 and −0.46 V, respectively. These indicated the improvement of electrocatalytic ability of zinc ferrite compared with those hematite structures.[49,50] As shown in the insets of Figure 6, the calibration curves depicted the amperometric response of the modified electrodes to H_2O_2 in PBS. These as-made sensors presented linear responses to H_2O_2 concentrations in the experimental range, with correlation coefficients of $r = 0.998$ and 0.999 for $ZnFe_2O_4$ CNCs and NPs, respectively. On the basis of these experiments, it is suggested that the electrochemical sensor containing dispersed NPs had a larger surface area accessible for H_2O_2 molecules than that of CNCs,[48−50] which explained that 11.6 nm NPs-based sensor showed higher catalytic activity than submicrometer CNCs-based sensor.

To verify the effect of the crystal size on the electrochemical sensing performance, NPs with the size of 20.5 nm were used in the electrochemical reduction of H_2O_2. The corresponding maximum peak current was 13.2 μA under the same experimental conditions (Figure S4), which showed the worst electrocatalytic activity among the used $ZnFe_2O_4$ electrodes. This confirmed that smaller single crystalline NPs displayed more active sites for the reduction of H_2O_2 than the larger well-crystalline ones. It should be pointed out that the reduction peak for NPs-based electrodes was much sharper than that of CNCs-modified electrodes. This indicated that the crystallization of the nanosheets and their ordered assembly in $ZnFe_2O_4$ CNCs had important influences on the electrochemical sensing properties of CNCs-modified electrodes.[27]

dx.doi.org/10.1021/la401627x | Langmuir 2013, 29, 8997−9003

4. CONCLUSION

Size-tunable $ZnFe_2O_4$ nanoparticles can be synthesized solvothermally using a mixed glycerol/water solvent while submicrometer $ZnFe_2O_4$ colloidal nanocrystal clusters are obtained when ethylene glycol is used as the solvent. Thus, obtained $ZnFe_2O_4$ nanoparticles are of a single crystalline phase with ferromagnetic properties. The saturation magnetization, remnant, and coercivity values of such nanoparticles increase with particle size. However, submicrometer nanocrystal clusters possess superparamagnetic properties with a relative large saturation magnetization value. Mechanistic study suggested that the hydrolysis of metal ions in the synthesis system plays an important role in the formation of spinel nanoparticles. The formation of the colloidal nanocrystal clusters was due to the self-assembly of crystalline $ZnFe_2O_4$ nanosheets into spherical cluster in highly preferred orientations. The particle size and structure of the colloidal nanocrystal clusters and nanoparticles play important roles in their sensing properties toward the electrochemical catalysis of H_2O_2 in a physiological system. These results presented in this paper are helpful for the controlled synthesis of targeted magnetic nanomaterials by rational design.

■ ASSOCIATED CONTENT

Supporting Information

Figures S1−S4. This material is available free of charge via the Internet at http://pubs.acs.org.

■ AUTHOR INFORMATION

Corresponding Author

*E-mail guopz77@yahoo.com (P.G.), pzguo@qdu.edu.cn (P.G.); yqwang@qdu.edu.cn (Y.W.); Tel +86-532-85951290; Fax +86-532-85955529.

Notes

The authors declare no competing financial interest.

■ ACKNOWLEDGMENTS

This work was financially supported by the National Natural Science Foundation of China (No. 21143006 and U1232104), the National High Technology Research and Development Program of China (2012AA110407), the Foundation of Qingdao Municipal Science and Technology Commission (11-2-4-2-(8)-jch), the Natural Science Foundation for Outstanding Young Scientists in Shandong Province (No. JQ201002), and the Foundation of "Taishan Scholar" program of Shandong Province, China.

■ REFERENCES

(1) Laurent, S.; Forge, D.; Port, M.; Roch, A.; Robic, C.; Elst, L. V.; Muller, R. N. Magnetic Iron Oxide Nanoparticles: Synthesis, Stabilization, Vectorization, Physicochemical Characterizations, and Biological Applications. *Chem. Rev.* **2008**, *108*, 2064−2110.

(2) Ida, S.; Yamada, K.; Matsunaga, T.; Hagiwara, H.; Matsumoto, Y.; Ishihara, T. Preparation of p-Type $CaFe_2O_4$ Photocathodes for Producing Hydrogen from Water. *J. Am. Chem. Soc.* **2010**, *132*, 17343−17345.

(3) Xuan, S. H.; Wang, F.; Wang, Y.-X. J.; Yu, J. C.; Leung, K. C.-F. Facile Synthesis of Size-Controllable Monodispersed Ferrite Nanospheres. *J. Mater. Chem.* **2010**, *20*, 5086−5094.

(4) Burda, C.; Chen, X. B.; Narayanan, R.; El-Sayed, M. A. Chemistry and Properties of Nanocrystals of Different Shapes. *Chem. Rev.* **2005**, *105*, 1025−1102.

(5) Mathew, D. S.; Juang, R. S. An Overview of the Structure and Magnetism of Spinel Ferrite Nanoparticles and Their Synthesis in Microemulsions. *Chem. Eng. J.* **2007**, *129*, 51−65.

(6) Chen, J. P.; Sorensen, C. M.; Klabunde, K. J.; Hadjipanayis, G. C.; Devlin, E.; Kostikas, A. Size-Dependent Magnetic Properties of $MnFe_2O_4$ Fine Particles Synthesized by Coprecipitation. *Phys. Rev. B* **1996**, *54*, 9288−9296.

(7) Guo, P. Z.; Zhang, G. L.; Yu, J. Q.; Li, H. L.; Zhao, X. S. Controlled Synthesis, Magnetic and Photocatalytic Properties of Hollow Spheres and Colloidal Nanocrystal Clusters of Manganese Ferrite. *Colloids Surf., A* **2012**, *395*, 168−174.

(8) Ge, J. P.; Hu, Y. X.; Biasini, M.; Beyerann, W. P.; Yin, Y. D. Superparamagnetic Magnetite Colloidal Nanocrystal Clusters. *Angew. Chem., Int. Ed.* **2007**, *46*, 4342−4345.

(9) Bao, N. Z.; Shen, L. M.; Wang, Y. H. A.; Ma, J. X.; Mazumdar, D.; Gupta, A. Controlled Growth of Monodisperse Self-Supported Superparamagnetic Nanostructures of Spherical and Rod-Like $CoFe_2O_4$ Nanocrystals. *J. Am. Chem. Soc.* **2009**, *131*, 12900−12901.

(10) Verma, S.; Pravarthana, D. One-Pot Synthesis of Highly Monodispersed Ferrite Nanocrystals: Surface Characterization and Magnetic Properties. *Langmuir* **2011**, *27*, 13189−13197.

(11) Meng, Y. D.; Chen, D. R.; Jiao, X. L. Synthesis and Characterization of $CoFe_2O_4$ Hollow Spheres. *Eur. J. Inorg. Chem.* **2008**, 4019−4023.

(12) Quickel, T. E.; Le, V. H.; Brezesinski, T.; Tolbert, S. H. On the Correlation Between Nanoscale Structure and Magnetic Properties in Ordered Mesoporous Cobalt Ferrite ($CoFe_2O_4$) Thin Films. *Nano Lett.* **2010**, *10*, 2982−988.

(13) Jia, Z. G.; Ren, D. P.; Liang, Y. C.; Zhu, R. S. A New Strategy for the Preparation of Porous Zinc Ferrite Nanorods with Subsequently Light-Driven Photocatalytic Activity. *Mater. Lett.* **2011**, *65*, 3116−3119.

(14) Mohapatra, S.; Rout, S. R.; Panda, A. B. One-Pot Synthesis of Uniform and Spherically Assembled Functionalized MFe_2O_4 (M = Co, Mn, Ni) Nanoparticles. *Colloids Surf., A* **2011**, *384*, 453−460.

(15) Glover, T. G.; Sabo, D.; Vaughan, L. A.; Rossin, J. A.; Zhang, Z. J. Adsorption of Sulfur Dioxide by $CoFe_2O_4$ Spinel Ferrite Nanoparticles and Corresponding Changes in Magnetism. *Langmuir* **2012**, *28*, 5695−5702.

(16) Li, Z. M.; Lai, X. Y.; Wang, H.; Mao, D.; Xing, X. J.; Wang, D. General Synthesis of Homogeneous Hollow Core−Shell Ferrite Microspheres. *J. Phys. Chem. C* **2009**, *113*, 2792−2797.

(17) Stjerndahl, M.; Andersson, M.; Hall, H. E.; Pajerowski, D. M.; Meisel, M. W.; Duran, R. S. Superparamagnetic Fe_3O_4/SiO_2 Nanocomposites: Enabling the Tuning of Both the Iron Oxide Load and the Size of the Nanoparticles. *Langmuir* **2008**, *24*, 3532−3536.

(18) Sun, S. H.; Zeng, H.; Robinson, D. B.; Raoux, S.; Rice, P. M.; Wang, S. X.; Li, G. X. Monodisperse MFe_2O_4 (M = Fe, Co, Mn) Nanoparticles. *J. Am. Chem. Soc.* **2004**, *126*, 273−279.

(19) Dong, H.; Li, X. L.; Peng, Q.; Wang, X.; Chen, J. P.; Li, Y. D. Monodisperse Magnetic Single-Crystal Ferrite Microsphere. *Angew. Chem., Int. Ed.* **2005**, *44*, 2782−2785.

(20) Wang, M.; Ai, Z. H.; Zhang, L. Z. Generalized Preparation of Porous Nanocrystalline $ZnFe_2O_4$ Superstructures from Zinc Ferrioxalate Precursor and Its Superparamagnetic Property. *J. Phys. Chem. C* **2008**, *112*, 13163−13170.

(21) Su, L.; Feng, J.; Zhou, Z.; Ren, C.; Li, H.; Chen, X. Colorimetric Detection of Urine Glucose Based $ZnFe_2O_4$ Magnetic Nanoparticles. *Anal. Chem.* **2012**, *84*, 5753−5758.

(22) Habibi, M. H.; Habibi, A. H.; Zendehdel, M.; Habibi, M. Dye-sensitized Solar Cell Characteristics of Nanocomposite Zinc Ferrite Working Electrode: Effect of Composite Precursors and Titania as a Blocking Layer on Photovoltaic Performance. *Spectrochim. Acta, Part A* **2013**, *110*, 226−232.

(23) Tahir, A. A.; Wijayantha, K. G. U. Photoelectrochemical Water Splitting at Nanostructured $ZnFe_2O_4$ Electrodes. *J. Photochem. Photobiol. A* **2010**, *216*, 119−125.

(24) Jun, Y. W.; Lee, J. H.; Cheon, J. Chemical Design of Nanoparticle Probes for High Performance Magnetic Resonance Imaging. *Angew. Chem., Int. Ed.* **2008**, *47*, 5122−5135.
(25) Tanaka, K.; Narita, A.; Kitamura, N.; Uchiyama, W.; Morita, M.; Inubushi, T.; Chujo, Y. Preparation for Highly Sensitive MRI Contrast Agents Using Core/Shell Type Nanoparticles Consisting of Multiple SPIO Cores with Thin Silica Coating. *Langmuir* **2010**, *26*, 11759−11762.
(26) Jun, Y. W.; Seo, J. W.; Cheon, A. Nanoscaling Laws of Magnetic Nanoparticles and Their Applicabilities in Biomedical Sciences. *Acc. Chem. Res.* **2008**, *41*, 179−189.
(27) Lu, Z. D.; Yin, Y. D. Colloidal Nanoparticle Clusters: Functional Materials by Design. *Chem. Soc. Rev.* **2012**, *41*, 6874−6887.
(28) Zhang, Z. L.; Wang, Y. H.; Tan, Q. Q.; Zhong, Z. Y.; Su, F. B. Facile Solvothermal Synthesis of Mesoporous Manganese Ferrite ($MnFe_2O_4$) Microspheres as Anode Materials for Lithium-Ion Batteries. *J. Colloid Interface Sci.* **2013**, *398*, 185−192.
(29) Cui, L. J.; Guo, P. Z.; Zhang, G. L.; Li, Q.; Wang, R. Y.; Zhou, M.; Ran, L. N.; Zhao, X. S. Facile Synthesis of Cobalt Ferrite Submicrospheres with Tunable Magnetic and Electrocatalytic Properties. *Colloids Surf., A* **2013**, *423*, 170−177.
(30) Zhu, Y. F.; Zhao, W. R.; Chen, H. R.; Shi, J. L. A Simple One-Pot Self-Assembly Route to Nanoporous and Monodispersed Fe_3O_4 Particles with Oriented Attachment Structure and Magnetic Property. *J. Phys. Chem. C* **2007**, *111*, 5281−5285.
(31) Egerton, R. F. *Electron Energy Loss Spectroscopy in the Electron Microscope*; Plenum Press: New York, 1996.
(32) Li, Y. B.; Yi, R.; Yan, A. G.; Deng, L. W.; Zhou, K. C.; Liu, X. H. Facile Synthesis and Properties of $ZnFe_2O_4$ and $ZnFe_2O_4$/Polypyrrole Core-Shell Nanoparticles. *Solid State Sci.* **2009**, *11*, 1319−1324.
(33) He, T.; Chen, D. R.; Jiao, X. L. Controlled Synthesis of Co_3O_4 Nanoparticles Through Oriented Aggregation. *Chem. Mater.* **2004**, *16*, 737−743.
(34) Banfield, J. F.; Welch, S. A.; Zhang, H. Z.; Ebert, T. T.; Penn, R. L. Aggregation-Based Crystal Growth and Microstructure Development in Natural Iron Oxyhydroxide Biomineralization Products. *Science* **2000**, *289*, 751−754.
(35) Alivisatos, A. P. Naturally Aligned Nanocrystals. *Science* **2000**, *289*, 736−737.
(36) Gong, J.; Li, G.; Tang, Z. Self-Assembly of Noble Metal Nanocrystals: Fabrication, Optical Property, and Application. *Nano Today* **2012**, *7*, 564−585.
(37) Tang, Z.; Kotov, N. A.; Giersig, M. Spontaneous Organization of Single CdTe Nanoparticles into Luminescent Nanowires. *Science* **2002**, *297*, 237−240.
(38) Zeng, H. C. Ostwald Ripening: A Synthetic Approach for Hollow Nanomaterials. *Curr. Nanosci.* **2007**, *3*, 177−181.
(39) Lin, J.; Lin, J.; Zhu, Y. F. Controlled Synthesis of the $ZnWO_4$ Nanostructure and Effects on the Photocatalytic Performance. *Inorg. Chem.* **2007**, *46*, 8372−8378.
(40) Ge, J. P.; Hu, Y. X.; Biasini, M.; Dong, C. L.; Guo, J. H.; Beyermann, W. P.; Yin, Y. D. One-Step Synthesis of Highly Water-Soluble Magnetite Colloidal Nanocrystals. *Chem.—Eur. J.* **2007**, *13*, 7153−7161.
(41) Cho, S.-B.; Noh, J.-S.; Park, S.-J.; Lim, D.-Y.; Choi, S.-H. Morphological Control of Fe_3O_4 Particles via Glycothermal Process. *J. Mater. Sci.* **2007**, *42*, 4877−4886.
(42) Li, F. S.; Wang, H. B.; Wang, L.; Wang, J. B. Magnetic Properties of $ZnFe_2O_4$ Nanoparticles Produced by a Low-Temperature Solid-state Reaction Method. *J. Magn. Magn. Mater.* **2007**, *309*, 295−299.
(43) Chinnasamy, C. N.; Narayanasamy, A.; Ponpandian, N.; Chattopadhyay, K.; Guérault, H.; Greneche, J.-M. Magnetic Properties of Nanostructured Ferrimagnetic Zinc Ferrite. *J. Phys.: Condens. Matter* **2000**, *12*, 7795−7805.
(44) Li, F. S.; Wang, H. B.; Wang, L.; Wang, J. B. Magnetic Properties of $ZnFe_2O_4$ Nanoparticles Produced by a Low-Temperature Solid-State Reaction Method. *J. Magn. Magn. Mater.* **2007**, *309*, 295−299.
(45) Li, Z.; Zhu, Z.; Liu, W.; Zhou, Y.; Han, B.; Gao, Y.; Tang, Z. Reversible Plasmonic Circular Dichroism of Au Nanorod and DNA Assemblies. *J. Am. Chem. Soc.* **2012**, *134*, 3322−3325.
(46) Zhu, Z.; Meng, H.; Liu, W.; Liu, X.; Gong, J.; Qiu, X.; Jiang, L.; Wang, D.; Tang, Z. Superstructures and SERS Properties of Gold Nanocrystals with Different Shapes. *Angew. Chem., Int. Ed.* **2011**, *50*, 1593−1596.
(47) Xia, Y.; Nguyen, T.; Yang, M.; Lee, B.; Santos, A.; Podsiadlo, P.; Tang, Z.; Glotzer, S. C.; Kotov, N. A. Self-Assembly of Self-Limiting, Monodisperse Supraparticles from Polydisperse Nanoparticles. *Nat. Nanotechnol.* **2011**, *6*, 580−587.
(48) Hu, X. L.; Yu, J. C.; Gong, J. M.; Li, Q.; Li, G. S. α-Fe_2O_3 Nanorings Prepared by a Microwave-Assisted Hydrothermal Process and Their Sensing Properties. *Adv. Mater.* **2007**, *19*, 2324−2329.
(49) Wang, X. H.; Zhang, L.; Ni, Y. H.; Hong, J. M.; Cao, X. F. Fast Preparation, Characterization, and Property Study of α-Fe_2O_3 Nanoparticles via a Simple Solution-Combusting Method. *J. Phys. Chem. C* **2009**, *113*, 7003−7008.
(50) Gong, J. M.; Wang, L. Y.; Zhao, K.; Song, D. D. One-step Fabrication of Chitosan−Hematite Nanotubes Composite Film and Its Biosensing for Hydrogen Peroxide. *Electrochem. Commun.* **2008**, *10*, 123−126.